Controllable synthesis of one-dimensional isolated $Ni_{0.5}Zn_{0.5}Fe_2O_4$ microtubes for application as catalyst support in RF heated reactors

Hua-nan Lv[1], Evgeny V. Rebrov[2,3], Peng-zhao Gao[1*], Rui-xue Ma[1], Zhou-li Lu[1], Jia Xu[1]

1 College of Materials Science and Engineering, Hunan University, Changsha, 410082, China

[2] School of Engineering, University of Warwick, Coventry, CV4 7AL, UK

[3] Department of Biotechnology and Chemistry, Tver State Technical University, 170026, Nab. A.Nikitina 22, Russia

Corresponding author: Peng-zhao Gao

Email: gaopengzhao7602@hnu.edu.cn Tel: +86 731 88822269; Fax: +86 731 88823554. (Peng-zhao Gao)

Abstract:

One-dimensional isolated $Ni_{0.5}Zn_{0.5}Fe_2O_4$ microtubes have been prepared via a template assisted sol-gel method. Temperature dependence of the structural and magnetic properties was studied via XRD, N_2 adsorption, SEM, TEM, and VSM. An increase in calcination temperature from 873 to 1273 K caused a decrease in the specific surface area from 80.7 to 17.0 m^2/g due to an increase of the grain size from 25.3 to 112 nm. All samples demonstrated anomalous coercivity behavior due to mechanical stresses acting on their domain walls. The porous microtubes calcined at 1073 K have a mean external diameter of 3.7 μm with a length-to-diameter ratio exceeding 12. The microtubes calcined at 973 K have the highest coercivity of 88.1 Oe and demonstrated the largest specific heating rate of 4.36 W/g in a radiofrequency field at 295 kHz.

Keywords: Ni-Zn ferrite; microtubes; magnetic properties; anomalous coercivity behavior; radio frequency heating.

1 Introduction

Recently, many researchers have studied the unusual morphologies of metal oxide, such as ordered porous particles, rods, fibers, and hollow structures as the performances of them depend on their chemical composition and surface properties as well as on their textural properties including morphology, surface area, pore volume, and pore dimensions [1-4]. In particular, hollow metal oxide with tubular structures have been extensively investigated because they offer advantages over other shapes, including a high surface area, narrow pore size distribution, light weight, and facilitates mass diffusion [5]. Specially, micro-tubes have important significance in the miniaturization of components and devices because of their small diameter and high slenderness ratio [6,7], and it's more suitable than nanotubes to load guest species such as biomolecule, catalyzer, nanoparticles for its larger microns in diameter, so it has unique applications in fields of drug delivery, catalysts loading and batteries and so on [8]. The currently used techniques for preparing hollow metal oxide structures include template approach, dry or wet spinning, electrospinning, and centrifugal spinning [8]. The template approach is very simple and cost-effective compared to the other methods [9]. Inspired by nature, hollow metal and metal oxide structures have already been produced employing butterfly wings [10], cotton fibers [11], cellulose acetate fibers [12] and paper [13] as templates.

In recent years, low-cost Ni–Zn ferrites were applied in high-frequency device applications due to their high values of chemical stability, magnetization, Curie temperature, permeability, and low power losses at high frequencies [14, 15]. They have an inverse spinel structure formed by a nearly close packed face centered cubic (FCC) array of anions with holes partly filled with cations, can be represented with

the formula $(Zn_xFe_{1-x})[Ni_{1-x}Fe_{1+x}]O_4$, in which Zn^{2+} ions locate in A interstitial (tetrahedral) sites, Ni^{2+} ions in B (octahedral) sites [16], and Fe^{3+} ions in the spinel lattice involve both tetrahedral A and octahedral B sites. The Ni–Zn ferrites have been prepared by co-precipitation, ball milling, spray pyrolysis, combustion synthesis, hydrothermal synthesis, and sol–gel methods [17-22]. As the microstructure and magnetic properties of ferrite materials are rather sensitive to the preparation method, some of those methods are not commercially viable due to disadvantages such as complexity, long synthesis time, or impurity penetration. Sol–gel is a flexible technique to adjust the properties of material by optimizing synthesis parameters such as hydrolysis time, temperature, precursor concentration and pH of the medium. The advantages of the sol–gel process include high purity of the resulting materials, their chemical homogeneity, and high degree of control over particle and grain size. Furthermore, the method can be easily scaled up to a large production scale which is crucial for the development of chemical processes involving radio frequency (RF) induced heating [15].

Combination of spinel ferrites with catalyst nanoparticles allows a novel process intensified platform for reactor system integration, in these composites, ferrites work as the susceptors of induction heating to provide efficient RF heating due to the adjustable Curie temperatures and moderate magnetic losses in the kHz range [23, 24], and catalyst loaded on the ferrites can work on some fine chemicals synthesis [16, 25]. RF heating provides efficient, fast and uniform heat transfer into catalytic sites and flowing fluid [26-29]. Base on the excellent textural properties, one-dimensional isolated spinel ferrites micro-tubes may be a good candidate loading the relative catalyst for the reactor system integration, while seldom literature reported on this field.

The goal of this study was to develop a method to prepare one dimensional isolated nickel zinc ferrite microtubes(NZF microtubes) by a template assisted sol-gel synthesis using natural cotton fibers as template. The influence of calcined temperature on the structural, magnetic and specific heating properties in a radiofrequency field of 295 kHz was investigated, Also the tested temperature dependence of magnetic and specific heating properties of the obtained NZF microtubes were studied.

2. Experimental process

2.1 Preparation of $Ni_{0.5}Zn_{0.5}Fe_2O_4$ microtubes

Ni-Zn ferrite microtubes with a nominal composition of $Ni_{0.5}Zn_{0.5}Fe_2O_4$ were prepared by the template assisted sol-gel synthesis [15, 30]. Solution A was prepared by dissolution of the corresponding metal nitrates in ethanol (all from Aldrich Co., ACS grade). Citric acid was dissolved in ethanol in a separate vessel to produce solution B which was added into solution A and the resulting mixture was stirred for 4 h. Then an ammonia solution was added dropwise till a pH of 2.3-2.5, the mixture was stirred for 24 h and then it was absorbed by cotton fibers. These impregnated cotton fibers were dried in an oven at 353 K to get a Ni-Zn ferrite dry gel loaded by cotton fibers. The dry gel was calcined at 873, 973, 1073, 1173 or 1273 K for 1 h to produce the corresponding ferrite microtubes. The heating rate during calcination was 5 $K \cdot min^{-1}$ from room temperature to the desired temperatures followed by a dwelling interval of 1 h at that temperature [15]. The microtubes are labeled as NZF-T hereafter, where index T represents the calcination temperature in K.

2.2 Characterization of $Ni_{0.5}Zn_{0.5}Fe_2O_4$ microtubes

The phase composition of the as-prepared samples was determined using an *X*-ray diffractometer

(X'Pert PRO) with nickel filtered Cu K_α radiation produced at 40 kV and 27.5 mA, at a scanning rate of 5^o min^{-1} and a step of 0.02^o. The Scherrer equation was used to calculate the crystal size (*D*, nm*)* [30]. The $d_{(311)}$ interplanar spacing was determined from the position of the (311) peak using the Bragg equation. The lattice constant (*a*) was obtained using Bragg's diffraction equation for a cubic lattice given by Eq. 1 [31]:

$$a = \frac{\lambda\sqrt{h^2+k^2+l^2}}{2\sin\theta_{hkl}} \quad (1)$$

The morphology of the as-prepared samples was characterized by scanning electron microscopy (SEM, JSM-6700F, Jeol, Oxford) equipped with an energy dispersive spectrometer (EDS).

The specific surface area of the as-prepared samples was determined by nitrogen adsorption at 77 K on a Micromeritics NOVA 1000E nitrogen adsorption apparatus.

The magnetization curves of the as-prepared samples were measured by a vibrating sample magnetometer (Princeton Measurements Corporation MicroMag 3900 VSM) equipped with a 2 Tesla electromagnet at several temperatures in the range from 298 to 833 K. The saturation magnetization (M_s), remnant magnetization (M_r), coercivity (H_c) and hysteretic losses were evaluated from the magnetization curves.

Curie temperature (T_c) of the as-prepared samples was determined from the temperature dependence of magnetic moment measured with an applied magnetic field of 1.5 T in the 373-1273 K range, the temperature corresponding to the minimize value of *dM/dT* in M-T curve was T_c [32].

The RF induced heating properties of the as-prepared samples was measured at a external magnetic field with a frequency of 295 kHz and intensity of 500Oe, and the results was given as the specific heating rate(*SHR*) to a mixture of water and aimed samples. In these experiments, a slurry of ferrite sample (10 mg) in deionized water (80 mg) was placed in a quartz tube inserted along the center axis in a 50 mm RF coil connected to an EasyHeat RF system (Ambrell) operated at a current of 200 A. The slurry temperature was measured with a fiber optic sensor (FISO). The specific heating rate (SHR) was calculated from the initial (linear) part of temperature vs time curves taken into account the specific heat capacities of the ferrite and water in the slurry and their weight fractions (Eq. 2) [33].

$$SHR = \frac{m_1 Cp_1 + m_2 Cp_2}{m_1 + m_2} \frac{dT}{dt} \quad (2)$$

where, m_1 and m_2 stand for the weight of water and nickel ferrite, respectively. Cp_1 and Cp_2 are the specific heat capacity of water (4180 $J \cdot kg^{-1} \cdot K^{-1}$) and nickel ferrite (483 $J \cdot kg^{-1} \cdot K^{-1}$) [34], respectively. $\frac{dT}{dt}$ is the heating rate obtained from experiments.

3. Results and discussion

3.1 Phase indication of $Ni_{0.5}Zn_{0.5}Fe_2O_4$ microtubes

Figure 1 shows XRD spectra of $Ni_{0.5}Zn_{0.5}Fe_2O_4$ microtubes calcined at different temperatures. It can be seen clearly that the spinel phase is formed in the entire temperature range studied (873-1273 K). The peaks are indexed with the standard pattern reported in JCPDF cards (#52-0278 for $Ni_{0.5}Zn_{0.5}Fe_2O_4$). All

samples calcined below 1173 K show a sharp diffraction peak at 35.54^{o} 2 theta, which is ascribed to the (311) plane. However, other peaks are rather wide which indicates that the obtained material has low degree of crystallinity [15]. Also, a minor amount of impurity (hematite, JCPDF #87-1164, labeled as H in Figure 1) is detected due to small discrepancies in molar ratios of metal nitrates or the segregation of metal oxides during the drying step.

Please insert Figure 1 here

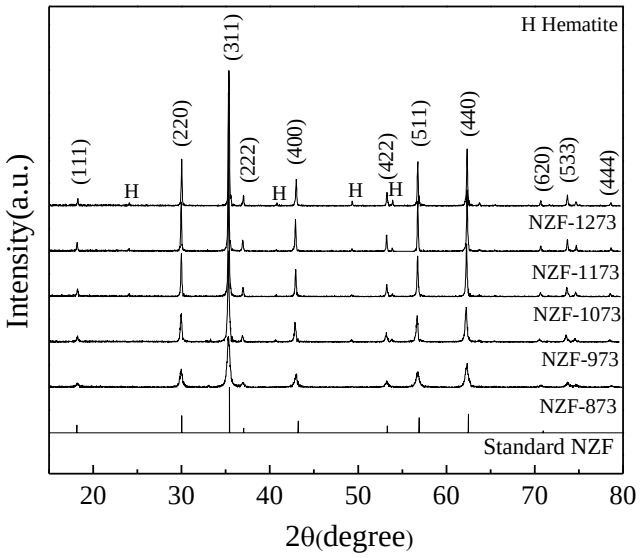

Figure 1. XRD patterns of the as-prepared $Ni_{0.5}Zn_{0.5}Fe_2O_4$ microtubes.

The unit cell parameter, interplanar spacing (d_{311}), average crystal size and specific surface area of the microtubes calcined at different temperatures are listed in Table 1. As the calcination temperature increases from 873 to 1273 K, the d_{311} spacing and unit cell parameter approach the corresponding values

for a bulk $Ni_{0.5}Zn_{0.5}Fe_2O_4$ material of 2.5330 and 0.8383 nm, respectively. The specific surface area decreases by a factor of nearly five due to progressive aggregation of small crystallites into larger particles. The average crystal size and specific surface area of the sample calcined at 1073 K are 73.6 nm and 44.3 m^2/g, respectively. The latter value is substantially higher than that previously reported for nickel zinc ferrites [15]. Namely, a highly porous structure is obtained in the template-assisted sol-gel method which greatly improves the specific surface area even it increases the average particle size at the same time.

Please insert Table 1 here

Table 1. Physical properties of $Ni_{0.5}Zn_{0.5}Fe_2O_4$ microtubes calcined at different temperatures.

Samples	NZF-873	NZF-973	NZF-1073	NZF-1173	NZF-1273
d_{311} interplanar spacing (nm)	2.5392	2.5391	2.5378	2.5363	2.5330
Unit cell parameter (nm)	0.8430	0.8429	0.8423	0.8423	0.8413
Average crystal size (nm)	25.3	37.2	73.6	95.4	112
Specific surface area (m^2/g)	80.7	63.7	44.3	29.4	17.0

3.2 Microstructure characterization and formation mechanism of $Ni_{0.5}Zn_{0.5}Fe_2O_4$ microtubes

Figure 2 shows characteristic SEM images of the template and $Ni_{0.5}Zn_{0.5}Fe_2O_4$ microtubes calcined at different temperatures. It can be seen that one-dimensional isolated ferrite microtubes are obtained. Their morphology and diameter as well as the ratio of length to diameter can be changed by increasing the calcination temperature. The template (cotton fiber) consists of a bundle of individual parallel fibers with

a vein-liked texture (Figure 2 (a, b)). The length of ferrite microtubes exceeds 40 μm (Figure 2(c)). The microtubes with a low degree of crystallinity are obtained after calcination at 873 K which agrees with the XRD data. Their mean diameter is 6 μm (Figure 2(d)). The microtubes with a mean diameter of 3.7± 0.2 μm and with a higher degree of crystallinity are obtained after calcination at 1073 K (Figure 2(e)). They are formed by rather uniform nanoparticles with a size of 80 nm and they have a higher length-to-diameter ratio of 12. After calcination at 1273 K, the microtubes with a mean diameter of 2.5 ± 0.2 μm are obtained. These highly crystalline samples are formed by much larger particles with a mean size of 120 nm (Figure 2(f)).

Please insert Figure 2 here

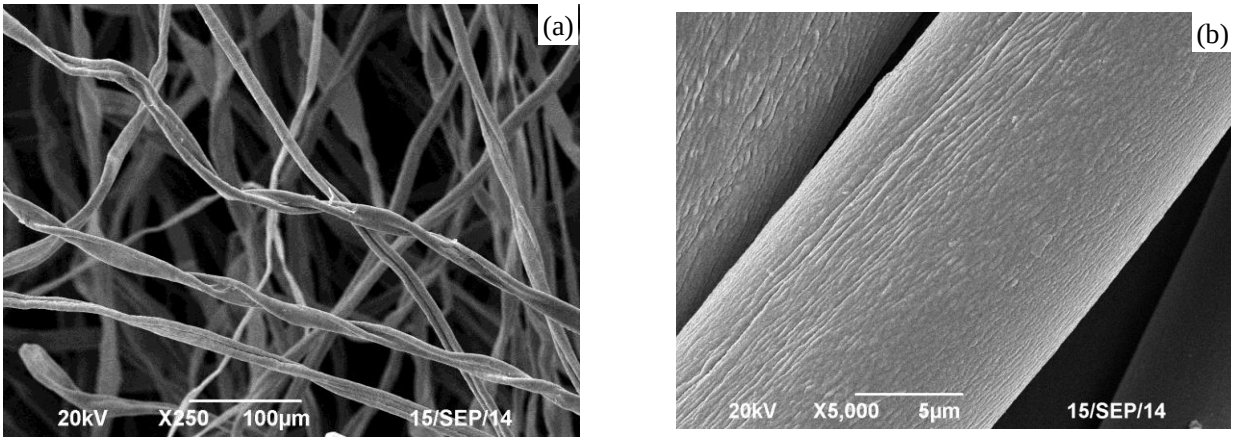

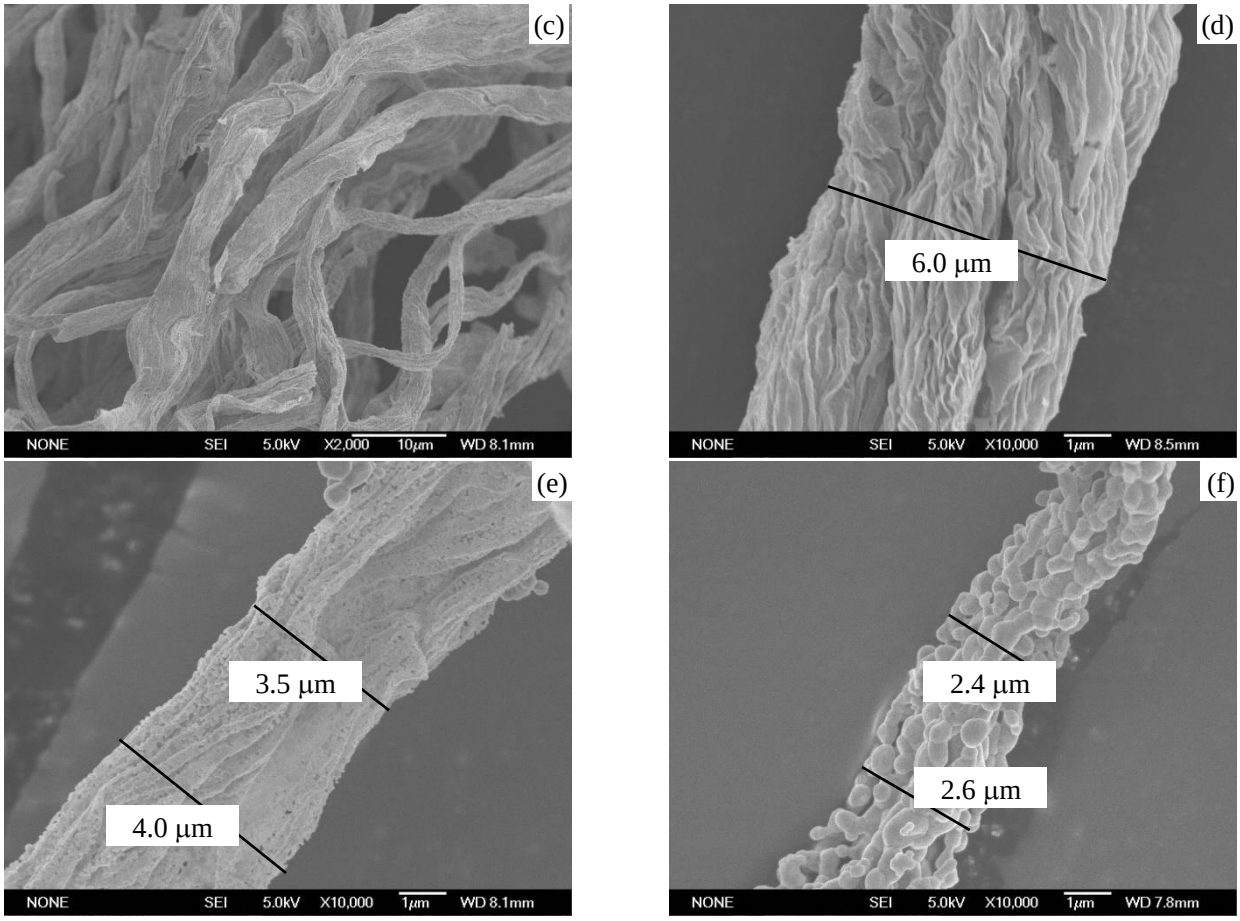

Figure 2. SEM images of (a, b) cotton fiber template soaked with the nickel ferrite sol and then dried to form a gel, (c, d) NZF-873; (e) NZF-1073; (f) NZF-1273 microtubes.

A characteristic feature of the fibers is the presence of small channels along the radial direction [35, 36]. Figure **3** (a) shows a characteristic SEM image of the template soaked with the nickel ferrite sol and then dried to form a gel. The elemental analysis data are listed in Table 2. The elemental composition of the template sample soaked with the nickel ferrite gel was determined at two different positions: near the center (point A, Figure 3a) and near the surface (point B, Figure 3a) of a cotton fiber. From these data, it can be concluded that the precursor sol penetrated about a few micron into the cotton fibers by capillary action.

In order to study the structure transition during calcination, characteristic SEM images of the microtubes calcined at different temperatures were taken (Figure 3(b-d)). As the temperature increases, the template and dry gel absorbed in the surface layer are decomposed causing an interfacial solid-state reaction and diffusion which yields interconnected ferrite particles. The tube diameter decreases after calcination at higher temperatures due to increased size of individual ferrite nanoparticles. One important issue for the formation of perfect microtubes is that an initial continuous layer of dry gel is mandatory.

Please insert Figure 3 here

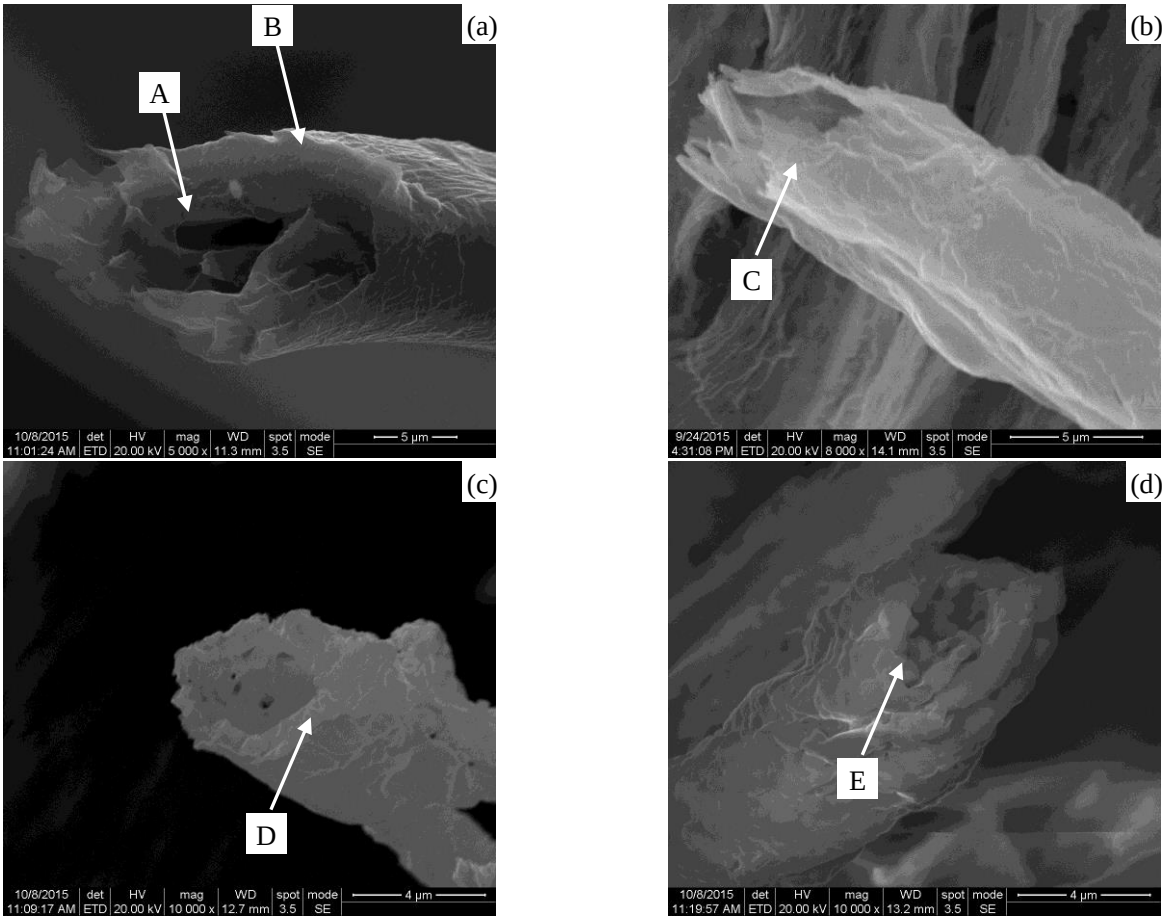

Figure **3**. SEM images of (a) cotton fiber template soaked with the nickel ferrite sol and then dried to form a gel, (b)

NZF-873; (c) NZF-1073; (d) NZF-1273 microtubes.

Please insert Table 2 here

Table 2 Elemental analysis data for different parts of the samples shown in Figure 3.

Point	Molar composition						Suggested composition	Reference
	C	O	N	Ni	Zn	Fe		
A	1.21	1.02	0.01	-	-	-	$C_6H_{10}O_5$	[36]
B	7.8	16.5	20.5	0.48	0.49	2.03	$(N_2H_5)_3Ni_{0.5}Zn_{0.5}Fe_2(N_2H_3\text{-}COO)_9$	[15]
C	0.1	4.08	-	0.51	0.49	2.01	$Ni_{0.5}Zn_{0.5}Fe_2O_4$, a small amount of C	[37]
D	-	4.03	-	0.50	0.51	2.02	$Ni_{0.5}Zn_{0.5}Fe_2O_4$	[37]
E	-	4.05	-	0.50	0.50	2.01	$Ni_{0.5}Zn_{0.5}Fe_2O_4$	[37]

Based on the experiment in which the template soaked with the nickel ferrite gel was converted into polycrystalline microtubes, it is possible to conclude that the reaction was surface mediated by template. This was related to a controlled preferential adsorption of the precursors in a thin outer layer of the cotton fibers and its very slow diffusion further inside the fibers during calcination. Figure 4 schematically shows the main steps in the formation of $Ni_{0.5}Zn_{0.5}Fe_2O_4$ microtubes. In the first step, the sol penetrated about a few microns into the cotton fibers by capillary action (Figure 4(a)). A higher amount of sol was accumulated near the outer surface of the fibers (Figure 4 (b)). As a result, an uneven distribution of gel particles along the radial direction of the fibers is obtained in the subsequent drying step (Figure 4 (c)). During the calcination step, small particles progressively aggregate and grow into larger aggregates. As

more particles exist near the surface of the templates fibers, the interconnection and growth of individual particles tends to form a relative dense structure, which transforms into tubular walls (Figure 4(d)). At the same time, there exist little particles in the center of the fiber. They are weakly connected connected to the walls and therefore they are removed when the template is removed during calcination.

Please insert Figure 4 here

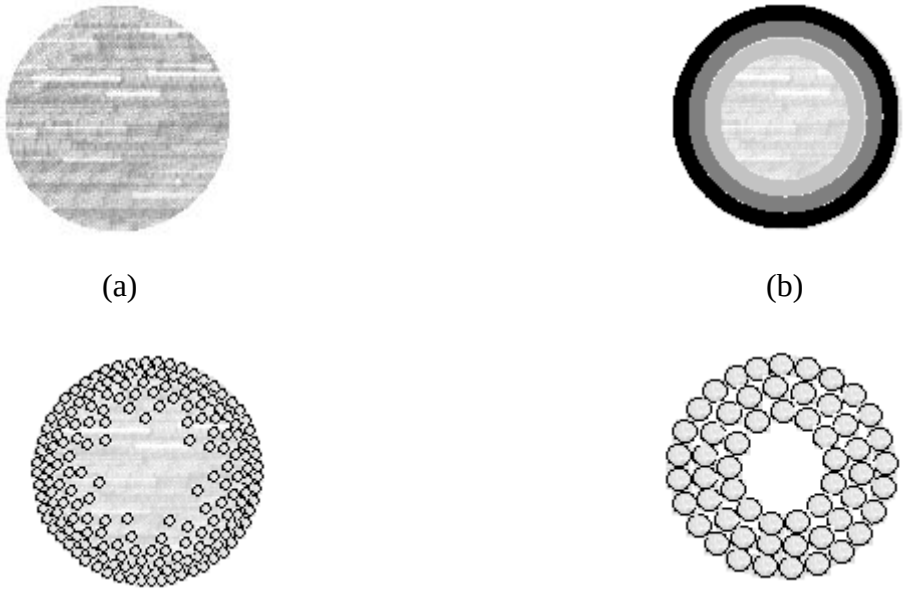

Figure 4. Schematic diagram of formation of $Ni_{0.5}Zn_{0.5}Fe_2O_4$ microtubes (cross section view).
(a) cotton fiber template, (b) cotton fiber template soaked with the nickel ferrite sol, (c) cotton fiber template with dry gel, (d) microtubes formed after calcination.

The individual nanoparticles can be seen in a TEM image (Figure 5). They have the shape of irregular polyhedrons with a mean size between 20 and 120 nm. It should be mentioned that the observed particle size is somehow larger than the crystallite size obtained from the XRD study due to the formation of

connecting necks between the two neighboring particles during calcination. No large aggregated nanoparticles are observed confirming much higher degree of dispersion as compared with a non-templated synthesis method [37]. Due to this fact, the specific area of the $Ni_{0.5}Zn_{0.5}Fe_2O_4$ microtubes was considerably enhanced in this study.

Please insert Figure 5 here

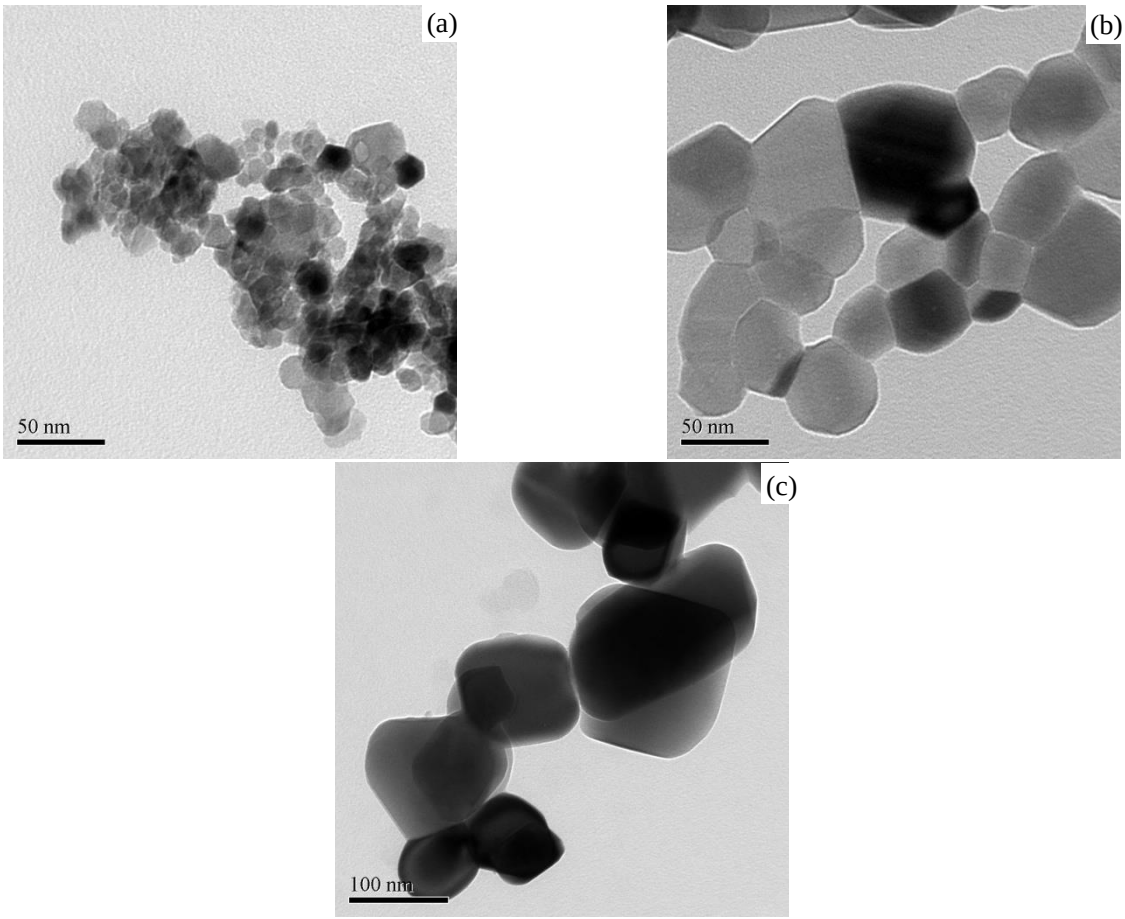

Figure **5**. TEM images of $Ni_{0.5}Zn_{0.5}Fe_2O_4$ microtubes calcined at different temperatures

(a) NZF-873; (b) NZF-1073; (c) NZF-1273.

3.3 Room temperature magnetic properties of $Ni_{0.5}Zn_{0.5}Fe_2O_4$ microtubes

A study of the magnetic properties was performed in order to determine if the samples possess specific magnetic properties and to look for possible effects of the structural transition during calcination on the thermal variation of saturation magnetization and coercivity. Room temperature hysteresis loops of the $Ni_{0.5}Zn_{0.5}Fe_2O_4$ microtubes calcined at different temperatures are shown in Figure 6 and their magnetic parameters are listed in Table 3.

Please insert Figure 6 here

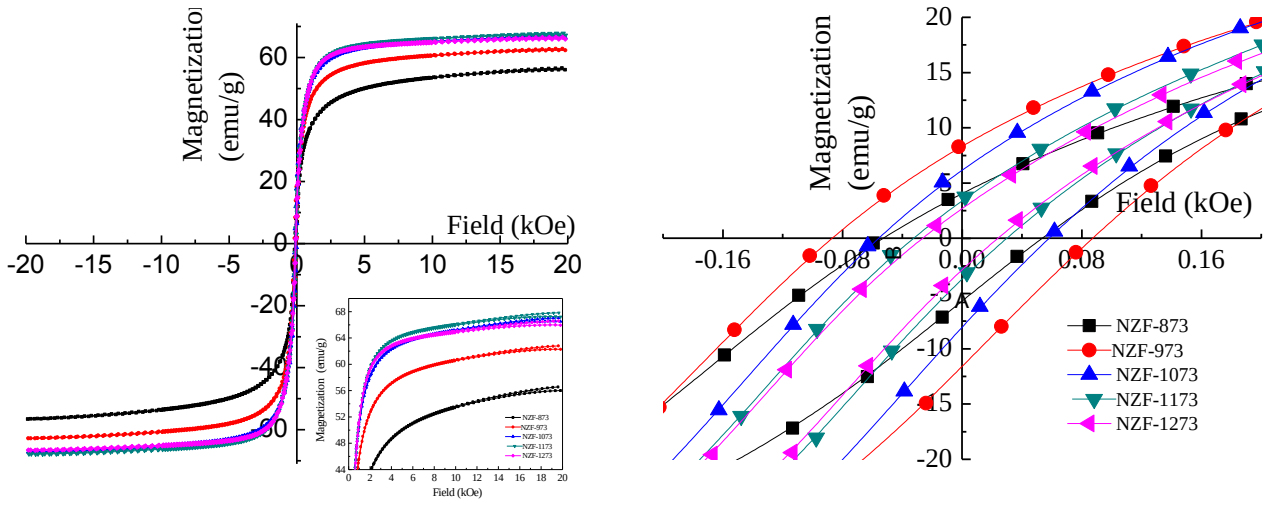

Figure **6**. (a) Magnetization curves of $Ni_{0.5}Zn_{0.5}Fe_2O_4$ microtubes calcined at different temperatures, (b) hysteresis loops of $Ni_{0.5}Zn_{0.5}Fe_2O_4$ microtubes at a larger magnification.

As the calcination temperature increases from 873 to 1273 K, the Curie temperature increases, however the saturation magnetization first increases and then remains virtually the same in the samples calcined above 1073 K. The remnant magnetization and coercivity monotonously decrease in the 973-

1273 K range. The maximum value of saturation magnetization exceeds that of the bulk Ni-Zn ferrite (56 emu/g) [38]. The saturation magnetization in nanoparticles is influenced by both the intrinsic (composition, preferential site occupancy of the cations, exchange effect) and extrinsic factors (microstructure and grain size) [39-41]. A relatively low value of saturation magnetization in NZF-873 can be explained by the existence of noncollinear spins at the surface. The exchange interaction between the Ni-Zn ferrite and the hematite impurity decreases the saturation magnetization in samples calcined at higher temperatures [40, 42]. At the same time, the increased mean crystal size increases saturation magnetization. The combined effect of exchange interaction and crystal size levels out therefore the saturation magnetization remains rather constant in the samples calcined above 1073 K.

Please insert Table 3 here

Table 3**.** Magnetic properties of $Ni_{0.5}Zn_{0.5}Fe_2O_4$ microtubes calcined at different temperatures.

Sample	NZF-873	NZF-973	NZF-1073	NZF-1173	NZF-1273
Saturation magnetization (emu/g)	56.6	62.8	67.8	67.1	66.6
Remnant magnetization (emu/g)	4.8	9.6	7.0	3.6	2.8
Coercivity (Oe)	56.9	88.1	56.6	31.4	26.1
Curie temperature (K)	532	534	535	537	549
ε_p (erg/cm^2) [a]	0.174	0.174	0.175	0.175	0.177
d_{cr} (nm) [b]	27.3	22.2	19.1	19.5	20.1
M_{SO} (emu/g) [c]	73.2	86.6	95.9	92.7	94.0
B (K$^{-1.5}$) [c]	5.05×10^{-5}	5.61×10^{-5}	5.74×10^{-5}	5.90×10^{-5}	5.59×10^{-5}
P (W/g) [d]	2.54	4.35	3.02	1.66	1.37
SHR at 295 kHz (W/g)	2.45	4.36	3.10	2.30	2.10

[a] calculated by Eq. 4,
[b] calculated by Eq. 3,
[c] calculated by Eq. 6,
[d] calculated by Eq. 7

Additional information regarding magnetic structure of the samples can be obtained by comparing the mean crystal size obtained by XRD with the critical magnetic domain size (d_{cr}) which is related to the transition from single to multidomain region [43]. The latter can be estimated by Eq. 3.

$$d_{cr} = \frac{9\varepsilon_p}{2\pi M_s^2} \qquad \text{(in CGS units)} \tag{3}$$

where M_s is the saturation magnetization (unit in G) and ε_p is the surface energy of the domain wall calculated by Eq. 4 [15].

$$\varepsilon_p = \left(\frac{2k_B T_C K_1}{a} \right)^{0.5} \tag{4}$$

where k_B is the Boltzmann constant (1.38×10^{-16} erg·K^{-1}), T_c the Curie temperature, a is the crystalline lattice constant, and K_1 is the absolute value of magnetocrystalline anisotropy constant. The anisotropy constant only slightly changes with composition at room temperature [15, 43], therefore the value reported by Srinivas et al. ($K_1 = 1.74\times10^4$ erg/cm^3 [44]) was used in this study.

Comparing the average crystal size (Table 1) with the critical domain size (Table 3), it can be seen that

NZF-873 has a single domain structure, i.e. composed of a single magnetic domain, while all other samples possess multidomain structure. The highest coercivity of 88.1 Oe is observed in NZF-973 as its grain size (37.2 nm) is only slightly above the critical size (22.2 nm). In the multidomain region, the coercivity decreases as the grain size increases from 37.2 to 120 nm (Table 1). The coercivity of crystallites with a size larger than the critical size of single domain (d_{cr}) is inversely proportional to the grain size (D) [45] (Eq. 5).

$$H_C^3 = \rho_c \frac{\sqrt{AK_1}}{M_S D} \quad (5)$$

where p_c is a dimensionless factor, A is the exchange constant.

Larger grain tends to contain a greater number of domain walls. The magnetization or demagnetization caused by domain wall movement requires less energy than that required by domain rotation. On contrast, with the contribution to magnetization or demagnetization due to domain rotation, the wall movement increases as the number of walls increases with increasing grain sizes [46]. Therefore, samples having larger grains are expected to have lower coercivity, and vice versa (Eq. 6). This seems to be the main reason for the changes in coercivity of the Ni–Zn ferrite microtubes.

As the calcination temperature increases, the Curie temperature of the microtube increases from 534 to 549 K (Table 3). A similar trend was observed by Sepelak et al. for nanostructured Mg ferrites [47]. These authors observed that Néel temperature (T_N) increases from 632 to 648 K with increasing annealing temperature from 1130 to 1280 K due to the cation reequilibration process. The increase in the

T_N with calcination temperature has also been observed in nanostructured $NiFe_2O_4$ [15].

3.4 Temperature dependence of magnetic properties of $Ni_{0.5}Zn_{0.5}Fe_2O_4$ microtubes

Figure 7 shows the temperature dependence of the saturation magnetization, remnant magnetization and coercivity of the $Ni_{0.5}Zn_{0.5}Fe_2O_4$ microtubes. As the temperature increases, the saturation and remnant magnetization monotonously decrease (Figure 7a and b). No remnant magnetization is observed above the Curie temperature (T_c) in samples calcined at 873 and 973 K. This indicates that the samples are superparamagnetic with a blocking temperature (T_B) less than or equal to the T_C. The samples calcined above 1073 K demonstrated a non-zero remnant magnetization above their Curie temperature which is due to their paramagnetic properties.

The tested temperature dependence of saturation magnetization is described by the Bloch law (Eq.6) [48]:

$$M_s = M_{S0}\,(1\text{-}BT^{1.5}) \qquad (6)$$

where M_{S0} is the saturation magnetization at $T = 0$ K, B is the Bloch constant [49]. The M_{S0} magnetization increases with calcination temperature till 1073 K and then remains relatively constant (Table 3). For the present microtubes, the range of prefactor B values of $(5.1\text{-}5.9)\times10^{-5}$ $K^{-1.5}$ obtained from the fitting procedure is close to the value of 7.5×10^{-5} $K^{-1.5}$ obtained for isolated nanoparticles [15]. The similarity of prefactor B values in the microtubes and individual nanoparticles can be understood from their

common crystal structure, their close lattice parameters (0.841-0.843 nm in this study vs 0.840 nm in Ref [15]) and their similar Curie temperatures.

The coercivity of all samples expresses a non-monotonous temperature dependence with a local maximum in the range between 573 and 823 K, which is slightly above their Curie temperature (Figure 7c). The absolute values of coercivity of the NZF-1073 of 40 and 35 Oe measured at 373 and 423 K are close to those of Ni-Zn ferrite nanoparticles calcined at 1073 K (42 and 39 Oe, respectively [15]). Below the Curie temperature, the coercivity decreases with an increase in temperature in accordance with the ferromagnetism theory as the degree of atomic thermal vibration increases [50]. Above the Curie temperature, an internal induced magnetic field is formed via a preferred orientation of the magnetic moments in the microtubes in the direction opposite to that of the applied magnetic field. The magnitude of this effect is proportional to the magnetic susceptibility, which decreases with temperature resulting in a decrease of coercivity [51].

However such coercivity behavior cannot be accounted for by exclusively considering the temperature dependence. The characteristic internal stress patterns in the nearly free standing microtubes may also result in the anomalous coercivity behavior since the internal stress induces anisotropy in the microtubes. The presence of temperature-dependent mechanical stresses acting on the domain walls must be considered as a cause of the observed behavior.

Please insert Figure 7 here

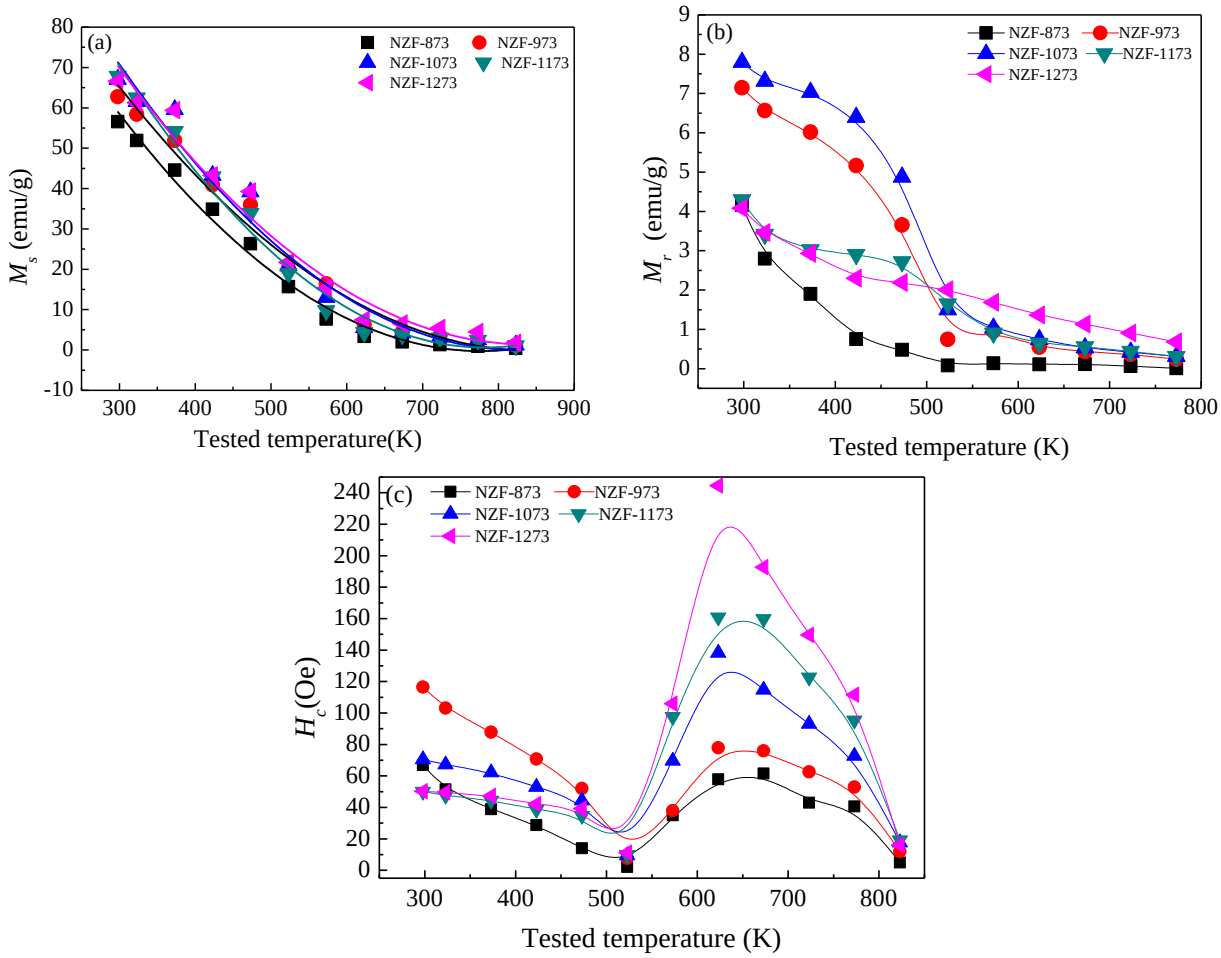

Figure **7**. (a) Saturation magnetization, (b) remnant magnetization, (c) coercivity of $Ni_{0.5}Zn_{0.5}Fe_2O_4$ microtubes as a function of temperature. Symbols represent experimental data. Solid lines in (a) represent predictions by Eq. 5. Solid lines in (b) and (c) are guides for the eye.

From the viewpoint of application of the obtained materials in catalytic reactors under radiofrequency heating, it is important that they possess high specific surface area and demonstrate high specific heating rate which allows to maintain desired temperature inside the reactor. As it was mentioned above, the materials obtained at 873 and 973 K demonstrated the highest specific surface area. Their specific heating

rate is another important factor in evaluating their potential for catalytic applications as susceptors of RF field [33, 51]. Hysteresis loss is the main mechanism of heating of $Ni_{0.5}Zn_{0.5}Fe_2O_4$ microtubes. The heat released is proportional to the area between the two magnetization curves. Figure 8 shows hysteresis loss of the microtubes as a function of tested temperature. Due to a non-zero saturation magnetization and a moderate coercivity, the microtubes could be heated by RF heating in the temperature range above their Curie temperature. This is a unique feature of these materials which was not observed in the nanoparticles of the same phase composition.

The hysteresis loss can be approximated as a function of coercivity and saturation magnetization following the approach developed in our previous study [15]:

$$P = C_0 \cdot H_c \cdot M_s \quad (7)$$

where C_0 is a constant.

Please insert Figure 8 here

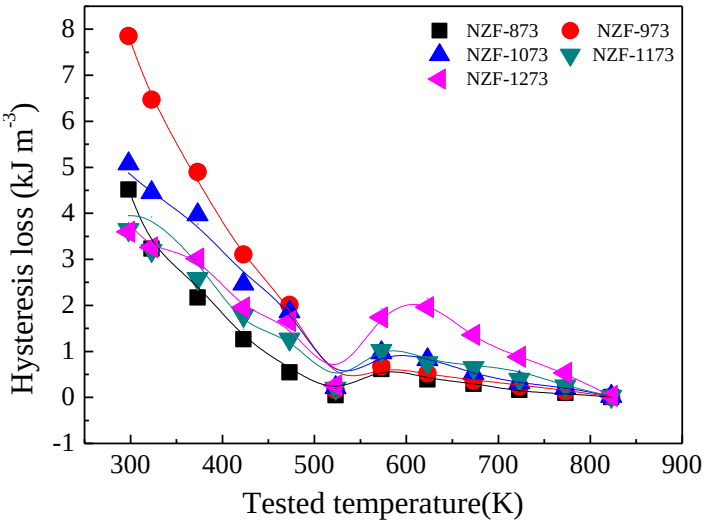

Figure 8. Hysteresis loss of the ferrite microtubes as a function of tested temperature.

Symbols represent experimental data. Solid lines are the guide for the eye.

The P values and the corresponding specific heating rates are listed in Table 3. It can be seen that the heating rate of three samples: NZF-873, NZF-973 and NZF-1073 can be predicted with a high degree of accuracy from their coercivity and saturation magnetization. However, the coercivity drops by a factor of 3 in NZF-1173 and NZF-1273 as compared to its maximum value observed in NZF-973, while their saturation magnetization remains rather constant as it was discussed above. The heating rate decreases only by a factor of 2. In other words, the heating rate determined from hysteresis loops becomes smaller than that measured directly by calorimetry which proved that it was Néel relaxation that contributed to the heating effect. The average crystal size in NZF-1173 and NZF-1273 (95.4 and 112 nm, respectively) is much bigger than the critical domain size (20 nm) so these two samples have a multidomain structure with a bulk-like behavior.

4. Conclusions

One dimensional isolated $Ni_{0.5}Zn_{0.5}Fe_2O_4$ microtubes with the length exceeding 40 μm and with high specific area and magnetic saturation have been prepared by a template-assisted sol-gel method. The possible formation mechanism of $Ni_{0.5}Zn_{0.5}Fe_2O_4$ microtubes was proposed. The formation of microtubes was attributed to the inhomogeneous infiltration of the precursor sol to a cotton fiber template. An increase in calcination temperature caused the decrease of diameter and specific surface area of microtubes while the average crystal size and the Curie temperature increased. The coercivity expressed a non-monotonous temperature dependence caused by mechanical stresses acting on the magnetic domain walls. While hysteresis loss was the main heating mechanism in all samples, Néel relaxation contributed to the heating effect in the samples with the mean particle size above 95 nm. The sample with a mean particle size of 37 nm demonstrated the best combination of specific surface area and the largest specific heating rate in RF field of 295 kHz.

5. Acknowledgements

The financial support from the Science and Technology Planning Project of Hunan Province, China (2012WK3023), the Royal Academy of Engineering for research exchanges with China and India–Major Award (2011-2012), the European Research Council (project 279867, “RF-enhanced microprocessing for fine chemicals synthesis using catalysts supported on magnetic nanoparticles, RFMiFiCS”), and the Russian Science Foundation (project 15-13-20015) is gratefully acknowledged.

References

[1] B. Boury, R.G. Nair, S.K. Samdarshi, T. Makiabadia, P.H. Mutina, Non-hydrolytic synthesis of hierarchical TiO_2 nanostructures using natural cellulose materials as both oxygen donors and template, New J. Chem. 36 (2012) 2196-200.

[2] V.F. Solovyov, L.-J. Wu, M.W. Rupich, S. Sathyamurthy, X. Li, Q. Li, Two-stage epitaxial growth of vertically-aligned SnO_2 nano-rods on (001) ceria, J. Cryst. Growth 408 (2014) 107-111.

[3] A.K. Gain, L. Zhang, W. Liu, Microstructure and material properties of porous hydroxyapatite-zirconia nanocomposites using polymethyl methacrylate powders, Mater. Design 67 (2015) 136-144.

[4] K.-J. Hwang, C.-H. Hwang, I.-H. Lee, T. Kim, S. Jin, J.-Y. Park, Synthesis and characterization of hollow metal oxide micro-tubes using a biomaterial template, Biomass Bioenergy 68 (2014) 62-66.

[5] N. Bao, Z. Wei, Z. Ma. Si-doped mesoporous TiO_2 continuous fibers: preparation by centrifugal spinning and photocatalytic properties, J. Hazard. Mater. 174 (2010) 129-136.

[6] H. Wang, S. Zhang, T. Liu, Preparation and application of micro-tubes, Chem. World (China) 12 (2005) 52-56.

[7] Y. Ma, C. Xiong, W. Huang, J. Zhao, X. Li, Q. Fan, W. Huang, Preparation of carbon microtubes by carbonizing the fluff of chinar Tree and their application as supercapacitor electrodes, Chin. J. Inorg. Chem. 3 (2012) 546-550.

[8] Xia Yu, Preparation and properties of fluorescent microtubes based on polyoxometalates, Northeast Normal University(China), Doctor degree thesis(in Chinese), 2013.11.

[9] P. Song, Q. Wang, Z. Zhang, Z. X. Yang, Synthesis and gas sensing properties of biomorphic $LaFeO_3$ hollow fibers templated from cotton, Sens. Actuators. B 147 (2010) 248-254.

[10] W. Peng, X. Hun, Di Zhang, Bioinspired fabrication of magneto-optic hierarchical architecture by Hydrothermal process from butterfly wing. J. Magnet. Magnet. Mater. 304 (2006) 197–202.

[11] P. Song, Qi Wang, Z. Yang, Biomorphic synthesis and gas response of In_2O_3 microtubules using cotton fibers as templates, Sens. Actuators. B, 168 (2012) 421-428.

[12] C. Zeng, P. Li, L. Zhang, Preparation of magnetic nickel hollow fibers with a trilobe structure using cellulose acetate fibers as templates, Appl, Surf, Sci. 266 (2013) 214-218.

[13] J. Li, F.-L. Kwong, H. L. N. Dickon, Synthesis of a biomorphic molybdenum trioxide templated from paper, J. Am. Ceram. Soc. 91 (2008) 1350-1353.

[14] Z. Peng, X. Fu, H. Ge, Z. Fu, C. Wang, L. Qi, H. Miao, Effect of Pr^{3+} doping on magnetic and dielectric properties of Ni–Zn ferrites by one-step synthesis, J. Magnet.Magnet. Mater. 323 (2011) 2513–2518.

[15] P. Gao, X. Hua, V. Degirmenci, D. Rooney, M. Khraisheh, R. Pollard, R.M. Bowman, E. V. Rebrov., Structural and magnetic properties of $Ni_{1-x}Zn_xFe_2O_4$ (x=0, 0.5 and 1) nanopowders prepared by sol–gel method, J. Magnet. Magnet. Mater. 348 (2013) 44-50.

[16] P. Gao, E.V. Rebrov, T.M.W.G.M. Verhoeven, J.C. Schouten, R. Kleismit, G. Kozlowski, J. Cetnar, Z. Turgut, G. Subramanyam, Structural investigations and magnetic properties of sol–gel $Ni_{0.5}Zn_{0.5}Fe_2O_4$ thin films for microwave heating, J. Appl. Phys. 107 (2010) 044317:1-7.

[17] S.J. Azhagushanmugam, N. Suriyanarayanan, R. Jayaprakash, Synthesis and characterization of nanocrystalline $Ni_{(0.6)}$ $Zn_{(0.4)}$ Fe_2O_4 spinel ferrite magnetic material, Phys. Procedia 49 (2013) 44-48.

[18] Kh. Gheisari, Sh. Shahriari, S. Javadpour. Structure and magnetic properties of ball-mill prepared nanocrystalline Ni–Zn ferrite powders at elevated temperatures, J. Alloys Compd. 552 (2013)146-151.

[19] A. Sutka, G. Strikis, G. Mezinskis, A. Lusis, J. Zavickis, J. Kleperis, D. Jakovlevs, Properties of Ni–Zn ferrite thin films deposited using spray pyrolysis, Thin Solid Films 526 (2012) 65-69.

[20] V.V. Awati, S.M. Rathod, Sagar E. Shirsath, Maheshkumar L. Mane, Fabrication of Cu^{2+} substituted nanocrystalline Ni–Zn ferrite by solution combustion route: Investigations on structure, cation occupancy and magnetic behavior, J. Alloys Compd. 553 (2013) 157-162.

[21] U. Wongpratat, S. Meansiri, E. Swatsitang, Local structure and magnetic property of $Ni_{1-x}Zn_xFe_2O_4$ (x = 0, 0.25, 0.50, 0.75, 1.00) nanoparticles prepared by hydrothermal method, Microelectronic Eng. 126 (2014) 19-26.

[22] Y. Liu, J.-J. Li, F.-F. Min, J.-Bo Zhu, M.-X. Zhang, Microwave-assisted synthesis and magnetic properties of $Ni_{1-x}Zn_xFe_2O_4$ ferrite powder, J Magnet Magnet Mater 354 (2014) 295-298.

[23] R. Benraba, H. Boukhlouf, A. Löfberg, A. Rubbens, R.-N. Vannier, E. BordesRichard, A. Barama, Nickel ferrite spinel as catalyst precursor in the dry reforming of methane: synthesis, characterization and catalytic properties, J. Nat. Gas. Chem. 21 (2012) 595–604.

[24] T.K. Houlding, E.V. Rebrov, Application of alternative energy forms in catalytic reactor engineering, Green Proces.

Synth. 1 (2012) 19–32.

[25] E.V. Rebrov, P. Gao, T.M.W.G.M. Verhoeven, J.C. Schouten, R. Kleismit, Z. Turgut, G. Kozlowski, Structural and magnetic properties of sol–gel $Co_{2x}Ni_{0.5-x}Zn_{0.5-x}Fe_2O_4$ thin films, J Magnet. Magnet. Mater. 323 (2011) 723–729.

[26] A. Ovenston, J.R. Walls, Generation of heat in a single catalyst pellet placed in an electromagnetic field for endothermic reforming of hydrocarbons, J Chem. Soc. Faraday Transactions 1: Phys. Chem. in Condens. Phases 79 (1983) 1073–1084.

[27] S.I. Al-Mayman, S.M. Al-Zahrani, Catalytic cracking of gas oils in electromagnetic fields: reactor design and performance, Fuel. Proces. Technol. 80 (2003) 169–182.

[28] P. Duquenne, A. Deltour, G. Lacoste, Application of inductive heating to granular media: temperature distribution in a granular bed, Int. J. Heat and Mass Trans. 36 (1993) 2473–2477.

[29] T.K. Houlding, K. Tchabanenko, M.T. Rahman, E.V. Rebrov, Direct amide formation using radiofrequency heating, Org. Biomol. Chem. 11 (2013) 4171–4177.

[30] P. Gao, B. Yan, D. Li, X. Gan, P. Li. W. Liu, Preparation and characterization of wire-liked $NiFe_2O_4$ nanoparticles with high specific area and excellent magnetic properties via a template-assembled sol-gel method, Key Eng. Mater. 633 (2015) 26-30.

[31] A.V. Raut, D.V. Kurmude, D.R. Shengule, K.M. Jadhav, Effect of gamma irradiation on the structural and magnetic properties of Co–Zn spinel ferrite nanoparticles, Mater. Res. Bull. 63 (2015) 123–128.

[32] Zhen-Fa Zi, Qiang-Chun Liu, Jian-ming Dai, Yan-kun Fu, Anomalous behavior of magnetic properties in $CoFe_2O_4$ ferrite nanoparticles (in Chinese). Sci Sin-Phys Mech Astron, 2012, 42: 242-248.

[33] T.K. Houlding, P. Gao, V. Degirmenci, K. Tchabanenko, E.V. Rebrov, Mechanochemical synthesis of $TiO_2/NiFe_2O_4$ magnetic catalysts for operation under RF field, Mater. Sci. Eng. B. 193 (2015) 175-180.

[34] K.B. Modi, S.J. Shah, N.B. Pujara, T.K. Pathak, N.H. Vasoya, I.G. Jhala, Infrared spectral evolution, elastic, optical and thermodynamic properties study on mechanically milled $Ni_{0.5}Zn_{0.5}Fe_2O_4$ spinel ferrite, J. Mol. Struct. 1049 (2013) 250-262.

[35] Tayebeh Fattahi Meyabadi, Fatemeh Dadashian, Gity Mir Mohamad Sadeghi, Hamid Ebrahimi Zanjani Asl, Spherical cellulose nanoparticles preparation from waste cotton using a green method, Powder Technol., 261 (2014) 232–240.

[36]Y. Xiaojiao. Study on the microstructure and fracture mechanism of kapok fiber[D]. Donghua University(China), Master degree thesis(in Chinese), 2015, 01

[37] B. Yan, P. Gao, Z. Lu, R. Ma, E.V. Rebrov, H. Zheng, Y. Gao. Effect of Pr^{3+} substitution on the microstructure, specific surface area, magnetic properties and specific heating rate of $Ni_{0.5}Zn_{0.5}PrxFe_{2-x}O_4$ nanoparticles synthesized via sol–gel method, J. Alloys Compd., 639(2015) 626-634.

[38] Q. Ma. Study on the preparation and magnetic properties of $Ni_{1-x}Zn_xFe_2O_4$ nanoparticles and composite with Co_3O_4. PhD thesis. Anhui University (China) (2013) 23-25.

[39] A.H Lu, E.L. Salabas, F. Schüth. Magnetic nanoparticles: Synthesis, protection, functionalization, and application, Angew. Chem. Int. Ed. 46 (2007) 1222-1244.

[40] A.L. Xia, C.H. Zuo, L.J. Zhang, C.X. Cao, Y. Deng, W. Xu, M.F. Xie, S.L. Ran, C.G. Jin, X.G. Liu, Magnetic properties, exchange coupling and novel stripe domains in bulk $SrFe_{12}O_{19}$/(Ni, Zn)Fe_2O_4 composites, J. Phys., D. 47 (2014) 415004.

[41] M.A. Gabal, Effect of Mg substitution on the magnetic properties of NiCuZn ferrite nanoparticles prepared through a novel method using egg white, J. Magnet. Magnet. Mater. 321 (2009) 3144-3148.

[42] M. Younas, M. Atif, M. Nadeem, M. Siddique, M. Idrees, R. Grossinger, Colossal resistivity with diminished tangent loss in Zn–Ni ferrite nanoparticles, J. Phys. D. 44 (2011) 345402

[43] I.Z. Rahman, T.T. Ahmed, A study on Cu substituted chemically processed Ni–Zn–Cu ferrites, J. Magnet. Magnet. Mater. 290–291 (2005) 1576-1579.

[44] Ch. Srinivas, B.V.Tirupanyam, A.Satish, V.Seshubai, D.L.Sastry, O.F.Caltun, Effect of Ni^{2+} substitution on structural and magnetic properties of Ni–Zn ferrite nanoparticles, J. Magnet. Magnet. Mater. 382(2015)15–19.

[45] D.S. Xue, G.Z. Chai, X.L. Li, X.L. Fan, Effects of grain size distribution on coercivity and permeability of ferromagnets, J. Magnet. Magnet. Mater. 320 (2008) 1541–43.

[46] A.C.F.M. Costa, E. Tortella, M.R. Morelli, R.H.G.A. Kiminami, Synthesis, microstructure and magnetic properties of Ni–Zn ferrites, J. Magnet. Magnet. Mater. 256 (2003) 174–182.

[47] V. Š epelák , D. Schultze , F. Krumeich , U. Steinike , K.D. Becker, Mechanically induced cation redistribution in magnesium ferrite and its thermal stability, Solid State Ionics 141-142 (2001) 677–682.

[48] M. Saidani , W. Belkacem, A. Bezergheanu, C.B. Cizmas, N. Mliki, Surface and interparticle interactions effects

on nano-cobalt ferrites, J. Alloys Compd. 653 (2015) 513-522.

[49] K. Maaz, A.Mumtaz, S.K.Hasanain, M.F.Bertino, Temperature dependent coercivity and magnetization of nickelferrite nanoparticles, J. Magnet. Magnet. Mater. 322 (2010) 2199–2202

[50] E.H. Frei, S. Shtrikman, D. Treves. Critical size and nucleation field of ideal ferromagnetic particles. Phys Rev 106 **(**1957) 446–455.

[51] S. Chatterjee, V. Degirmenci, F. Aiouache, E.V. Rebrov, Design of a radio frequency heated isothermal micro-trickle bed reactor, Chem. Eng. J. 243 (2014) 225–233.